*J. Fluid Mech.* (2013), *vol.* 727, *pp.* 56–82.  
doi:10.1017/jfm.2013.235

# Thixotropic gravity currents

**Duncan R. Hewitt**[1,†] **and Neil J. Balmforth**[2]

[1]Institute of Theoretical Geophysics, Department of Applied Mathematics and Theoretical Physics, University of Cambridge, Wilberforce Road, Cambridge, CB3 0WA, UK

[2]Department of Mathematics, University of British Columbia, Vancouver, BC, V6T 1Z2, Canada

(Received 12 February 2013; revised 15 April 2013; accepted 6 May 2013; first published online 14 June 2013)

We present a model for thixotropic gravity currents flowing down an inclined plane that combines lubrication theory for shallow flow with a rheological constitutive law describing the degree of microscopic structure. The model is solved numerically for a finite volume of fluid in both two and three dimensions. The results illustrate the importance of the degree of initial ageing and the spatio-temporal variations of the microstructure during flow. The fluid does not flow unless the plane is inclined beyond a critical angle that depends on the ageing time. Above that critical angle and for relatively long ageing times, the fluid dramatically avalanches downslope, with the current becoming characterized by a structured horseshoe-shaped remnant of fluid at the back and a raised nose at the advancing front. The flow is prone to a weak interfacial instability that occurs along the border between structured and de-structured fluid. Experiments with bentonite clay show broadly similar phenomenological behaviour to that predicted by the model. Differences between the experiments and the model are discussed.

**Key words:** complex fluids, gravity currents, non-Newtonian flows

## 1. Introduction

Thixotropic fluids have a time-dependent microstructure that gradually builds up when the fluid is at rest, leading to a slow increase in the effective viscosity, but is reversibly broken down by flow, thereby lowering the fluid's resistance (Mewis & Wagner 2009). A wide range of fluids exhibit thixotropic behaviour, including natural clay suspensions, industrial drilling fluids and cements, printing inks and paints, oils and grease, and food products such as mayonnaise and ketchup (Barnes 1997; Mewis & Wagner 2009). Two key features of thixotropic fluids have recently been identified (Coussot *et al.* 2002*a*,*b*; Bonn *et al.* 2004; Moller *et al.* 2009). First, they may experience a so-called 'viscosity bifurcation', describing the response of the fluid under a fixed applied stress: if the stress is less than a certain critical value, the fluid evolves to a structured ('jammed') or solid state of rest with a large or diverging viscosity. Above that threshold, however, the microstructure abruptly disintegrates, substantially lowering the viscosity and initiating extensive fluid flow. Crucially, the value of the critical stress depends on how long the fluid was left to age before the stress was applied. The second key feature is that once flow is initiated

† Email address for correspondence: drh39@cam.ac.uk

and microstructure broken down, such a state can only persist if the shear rate is maintained above another critical value; if the fluid flows in such a way that shear rates decline below this second threshold, the microstructure swiftly recovers and jams, abruptly increasing the viscosity and blocking flow.

Gravity currents form a particularly important class of flows in which such thixotropic effects can play a significant role. Many geophysical muds and clays appear to be thixotropic, and the relatively sudden and long runouts of mudslides and 'quick-clay' avalanches has been suggested to originate from this rheology (Khaldoun *et al.* 2009). In industrial settings, currents of mine tailings and waste mineral slurries have been observed to flow much further than predicted (Henriquez & Simms 2009; Simms *et al.* 2011), with potentially serious environmental consequences. On a different scale, household foodstuffs such as ketchup are often tested in the 'Bostwick consistometer' (a variant of the classical dambreak problem in which material is suddenly released and slumps down a channel; Balmforth *et al.* 2006*a*), yet the confounding role that thixotropy can play in such a device is usually ignored.

Important features of thixotropic gravity currents were documented in the experiments of Coussot *et al.* (2002*a*). These authors observed that a suspension of bentonite clay emplaced as a mound on an inclined plane did not flow provided the slope was below a certain critical angle. Above that angle, however, the mound collapsed dramatically, with a fraction of the clay flowing rapidly down the incline, and a horseshoe-shaped remnant of immobile material being left behind. The critical angle corresponds to the stress at which the viscosity bifurcation occurs, the avalanching fluid having de-structured and separated from the structured horseshoe-shaped remnant. For uniform layers on an inclined plane, Huynh, Roussel & Coussot (2005) showed that the critical angle increased if the fluid was left to rest and 'age' for longer. Similar 'avalanche' behaviour was recorded for dambreaks on inclined planes by Coussot *et al.* (2005) and for clay suspensions by Khaldoun *et al.* (2009). The latter authors also reported that the collapse was mediated by a thin de-structured basal layer, upon which the overlying rigid bulk of the material was conveyed.

Although previous work has proposed constitutive laws describing the viscosity bifurcations of thixotropic fluid (see § 2), there have been few attempts to couple such rheological models with the detailed flow dynamics. In particular, aside from a few computations reported by Coussot *et al.* (2005), there has been no attempt to model in detail the spatio-temporal evolution of a thixotropic gravity current on an inclined plane. Our aim in the current paper is to provide such a model; we present a shallow-layer theory that describes the release of a finite volume of thixotropic fluid on a slope. Such theories are well documented for Newtonian (Huppert 1982; Lister 1992) and viscoplastic (Liu & Mei 1989; Balmforth, Craster & Sassi 2002; Balmforth *et al.* 2006*b*) fluids.

Our rheological model, which accounts for the two key thixotropic effects outlined in the first paragraph above, is described in § 2. In § 3, we couple this rheology with lubrication theory for shallow flow. We solve the equations of the model numerically in section § 4, in both two and three dimensions, and discuss the main features of the flow. In § 5, we present experimental results for the gravity current of an aqueous suspension of bentonite clay. There is broad agreement between the theory and experiments, but there are also some notable differences, which are discussed here. Finally, in § 6 we summarize our main results. In exploring the theoretical model, we encounter a novel type of interfacial instability; additional details of this feature of the model are presented in the Appendix.

## 2. Rheological model

### 2.1. *Background*

Thixotropic rheology has been described using simple constitutive models that exploit a parameter, $\lambda(t)$, which describes the degree of internal structure (Barnes 1997; Mewis & Wagner 2009). The parameter lies in a range $[0, \lambda_0]$: the fluid has no effective microstructure if $\lambda = 0$, but is fully structured and solid-like when $\lambda = \lambda_0$. The structure parameter controls the viscosity $\mu(\lambda)$ in the generalized Newtonian-fluid model,

$$\tau_{ij} = \mu(\lambda)\,\dot{\gamma}_{ij}, \tag{2.1}$$

which relates the deviatoric stress tensor $\tau_{ij}$ to the tensor $\dot{\gamma}_{ij} = \partial u_i/\partial x_j + \partial u_j/\partial x_i$, which measures the rate of strain. In spatially uniform settings, the structure parameter is often taken to satisfy an evolution equation of the form

$$\frac{\mathrm{d}\lambda}{\mathrm{d}t} = g(\lambda, \dot{\gamma}) = G(\lambda, \tau), \tag{2.2}$$

where $\dot{\gamma} = \sqrt{\dot{\gamma}_{ij}\dot{\gamma}_{ij}/2}$ and $\tau = \sqrt{\tau_{ij}\tau_{ij}/2}$ denote tensor invariants, and $G(\lambda, \tau)$ follows from $g(\lambda, \dot{\gamma})$ on using (2.1). Various forms for $\mu(\lambda)$ and $g(\lambda, \dot{\gamma})$ have been proposed in the literature (Coussot *et al.* 2002*a*,*b*; Dullaert & Mewis 2006; Moller, Mewis & Bonn 2006; Alexandrou, Constantinou & Georgiou 2009; Putz & Burghelea 2009). In general, $g(\lambda, \dot{\gamma})$ contains a positive term corresponding to restructuring or 'healing', and a negative term proportional to $\dot{\gamma}$ describing the de-structuring effects of flow. The viscosity $\mu(\lambda)$ increases with structure, and becomes large or even diverges as the fluid becomes fully structured.

To illustrate how the thixotropic model above can account for the two key thixotropic effects outlined in the introduction, we use the quasi-steady version of (2.2), $G(\lambda, \tau) = 0$. The overall idea is that, for low or vanishing stress, $G(\lambda, \tau)$ is a positive, decreasing function of $\lambda$ that vanishes only for $\lambda = \lambda_0$ (figure 1*a*). As is clear from (2.2), $G(\lambda_0, \tau) = 0$ corresponds to a fully structured equilibrium state, which is stable as long as $\partial G(\lambda_0, \tau)/\partial\lambda < 0$. As the stress is increased, the curve representing $G(\lambda, \tau)$ is pushed down somewhere over the range of $\lambda$, eventually touching the $G(\lambda, \tau) = 0$ axis and creating two new equilibrium states, $\lambda = \lambda_\pm$, at a critical stress, $\tau = \tau_C$, which corresponds, via (2.2), to a critical strain rate $\dot{\gamma}_C$. The newly created state with less structure, $\lambda = \lambda_- < \lambda_+$, is stable, whilst that with an intermediate degree of structure, $\lambda = \lambda_+$, is unstable. However, the fully structured state $\lambda = \lambda_0$ persists during the creation of $\lambda_\pm$ and remains stable. This implies that fluid which had been prepared in the fully structured state before the stress was increased would remain in that state; only if the fluid was initially de-structured would $\lambda$ converge to $\lambda_-$.

If the stress is increased still further, the curve of $G(\lambda, \tau)$ continues to be driven downwards, and the unstable equilibrium moves to higher $\lambda$. Eventually, this state collides with the fully structured solution at $\lambda = \lambda_0$, rendering that equilibrium unstable ($\partial G(\lambda_0, \tau)/\partial\lambda$ becomes positive). This bifurcation occurs at stress $\tau = \tau_A$; for higher stresses $\tau \geqslant \tau_A$, the only stable equilibrium in the range $[0, \lambda_0]$ is $\lambda = \lambda_-$. Therefore, all structure disintegrates and evolves towards the de-structured equilibrium, even if the fluid were initially fully structured. The set of curves for increasing stress in figure 1(*a*) illustrate a sequence of such situations.

The behaviour of the structure function in figure 1(*a*) implies a hysteretic relation between stress $\tau$ and strain rate $\dot{\gamma}$ if the stress on a sample of fluid is first ramped up until flow occurs, and then decreased back down until the flow subsides. More

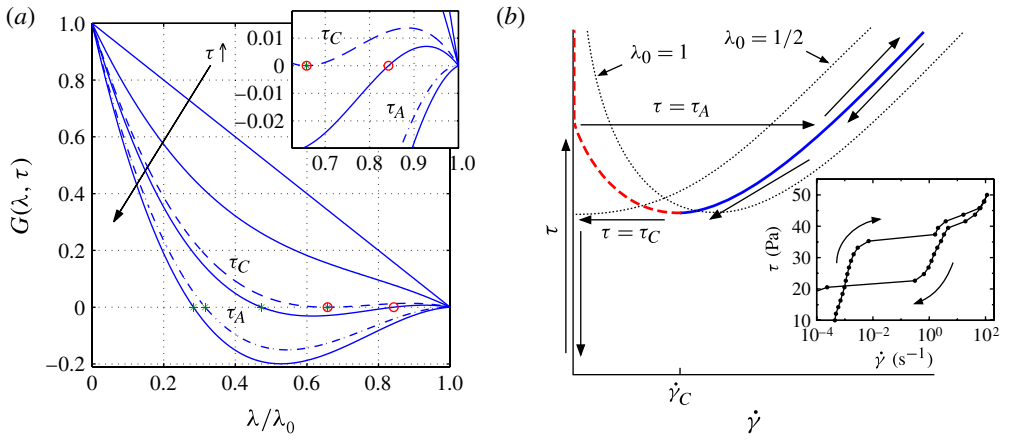


FIGURE 1. (Colour online) (*a*) The structure function $G(\lambda, \tau)$ for various values of the stress $\tau$. The curves are based on the model (2.4). The dashed and dot-dashed curves show the critical cases $\tau = \tau_C$ and $\tau = \tau_A$. Stars indicate the stable, less structured equilibrium states, and circles indicate the unstable, intermediate structured states. (*b*) A sketch of the hysteretic stress–strain-rate relation, with the arrows indicating the pathway expected for an experiment in which stress is first increased past the critical value $\tau_A$, and then decreased back below $\tau_C$. Non-zero strain rates below the critical value $\dot{\gamma}_C$ cannot be attained. The dashed line shows the unstable, intermediate structured equilibrium. The dotted lines show the stress–strain-rate relations for $\lambda_0 = 1/2$ (idealized yield-stress-like behaviour) and $\lambda_0 = 1$ ($\tau_A \to \infty$); these values are specific to our model (2.4). The inset shows rheometric data for a bentonite clay suspension (7.5 wt% $\approx$ 10 % by volume) in a cone-and-plate rheometer. The stress was increased from 10 to 50 Pa in 20 steps, and then decreased again, waiting for 5 s at each stress level. The fluid was pre-sheared for 2 min at 100 Pa, and left to rest for 5 min before starting the test.

specifically, as sketched in figure 1(*b*), the fluid is initially static and fully structured ($\lambda = \lambda_0$ and $\dot{\gamma} = 0$), and remains so until that state loses its stability at $\tau = \tau_A$. The fluid structure then disintegrates and evolves towards the less structured state $\lambda = \lambda_-$ with finite shear rate. If the stress is then reduced, the flowing, less structured state of the fluid is preserved until $\tau$ falls below $\tau_C$, at which juncture that state disappears. Thereafter, the flow can no longer destroy the microstructure at the same pace as it heals, and the fluid evolves back towards the structured state, with the viscosity abruptly increasing and the flow coming to a halt.

In other words, the viscosity bifurcation of Coussot *et al.* (2002*b*) occurs at $\tau = \tau_A$, and the second transition at $\tau = \tau_C$ corresponds to the shear rate falling below the critical threshold $\dot{\gamma}_C$ (see figure 1*b*). In terms of the thixotropic model, both transitions correspond to bifurcations in the sense of standard dynamical systems theory. Henceforth, we refer to both as 'viscosity bifurcations', even though the second does not strictly conform to the terminology of Coussot *et al.* (2002*b*).

### 2.2. *The rheological model*

Our aim is to present a simple model of thixotropic gravity currents. For the task, we incorporate the thixotropic rheology, and specifically the viscosity bifurcations, in as simple a manner as possible. More precisely, we use the structure function shown in figure 1(*a*) to relate the local stress to the microstructural state. That is, given the stress, we solve $G(\lambda, \tau) = 0$ to determine $\lambda$, and thence the viscosity, $\mu(\lambda)$.

A convenient form for the structure function is furnished by the models

$$g(\lambda, \dot{\gamma}) = \frac{(\lambda_0 - \lambda)}{\lambda_0 T} - \alpha\lambda\dot{\gamma} \quad \text{and} \quad \mu(\lambda) = \frac{\mu_0\lambda_0}{(1-\lambda)(\lambda_0 - \lambda)}, \tag{2.3a,b}$$

which imply

$$G(\lambda, \tau) = \frac{(\lambda_0 - \lambda)}{\lambda_0 T}\left[1 - \Gamma\lambda(1-\lambda)\tau\right] = 0, \tag{2.4}$$

where $T$ and $\alpha$ are positive empirical constants, $\mu_0$ is a constant reference viscosity and $\Gamma = \alpha T/\mu_0$. The first term on the right-hand side of (2.3*a*) can be interpreted as the healing of the microstructure back towards the fully structured state $\lambda = \lambda_0$, and the second term as the flow-induced de-structuring. The relationship between (2.3) and previous models is discussed in § 2.4 below.

Equation (2.4) can be solved analytically to give the three branches of the stress–strain-rate relation:

$$\lambda = \lambda_0, \quad \lambda = \lambda_\pm(\tau) = \frac{1}{2}\left[1 \pm \left(1 - \frac{4}{\Gamma\tau}\right)^{1/2}\right]. \tag{2.5a,b}$$

The points of bifurcation can also be determined analytically:

$$\tau_A = \frac{1}{\Gamma\lambda_0(1-\lambda_0)}, \quad \tau_C = \frac{4}{\Gamma}, \quad \dot{\gamma}_C = \frac{2\lambda_0 - 1}{\Gamma\mu_0\lambda_0}. \tag{2.6}$$

Over the range $\tau_C < \tau < \tau_A$, the stress–strain-rate relation has three possible solutions, raising the question of how to select the appropriate structural state given the stress. We dismiss the choice $\lambda = \lambda_+$, as this state corresponds to an unstable equilibrium. The selection between the other two options, $\lambda = \lambda_-$ and $\lambda = \lambda_0$, is dictated by the stress history of the fluid: if the material has never been subjected to a stress exceeding $\tau_A$, then the fluid structure has never disintegrated, and $\lambda = \lambda_0$. On the other hand, if the structure did disintegrate at some moment in the past (with $\tau > \tau_A$), then the fluid is in its less structured state, and $\lambda = \lambda_-$.

Note that our use of $G(\lambda, \tau)$ in this fashion corresponds to assuming that the disintegration of the microstructure for $\tau \geqslant \tau_A$, or restructuring for $\tau \leqslant \tau_C$, is instantaneous (as in a kind of rapid phase transition). The differential constitutive law in (2.2) allows for a more general version of the scenario, and in particular for delays in disintegration or restructuring. Hence, our model can be thought of as the quasi-steady version of (2.2). However, retaining the time rate of change of $\lambda$ in the rheological model complicates the theory significantly. On the other hand, constitutive laws are often little more than mathematical formulations of flow-curve cartoons based on a combination of physical intuition and rheometric data. Hence, it is not clear that (2.2) conveys much more physical realism that the statement $G(\lambda, \tau) = 0$. Indeed, when supplemented with the rules for selecting amongst the multiple branches of the stress–strain-rate relation, (2.4) can be viewed as a constitutive law in its own right.

### 2.3. *Ageing*

Rheological measurements (see e.g. Moller *et al.* 2009) suggest that the critical threshold for flow to begin, $\tau_A$, depends on the ageing time of the fluid $T_{age}$. This time scale can be of the order of several minutes or even hours, and is typically longer than the duration of a gravity current flowing down an incline in a laboratory experiment. We therefore make the assumption that, although ageing controls the

threshold for initiation of flow, it takes place too slowly to influence the dynamics of the gravity current.

We incorporate the effect of ageing into our model via the parameter $\lambda_0$. Specifically, the higher critical stress $\tau_A = [\Gamma\lambda_0(1-\lambda_0)]^{-1}$ increases with $\lambda_0$. Therefore, as shown in figure 1(*b*), when $\lambda_0 \to 1/2$, the hysteresis loop of the stress–strain-rate relation disappears, leaving a single-valued curve representing the stable equilibrium. This state is fully structured for $\tau < \tau_C = \tau_A = 4/\Gamma$, but de-structures and flows at higher stresses. That is, structure formation and disintegration take place at a common critical or yield value, the critical shear rate $\dot{\gamma}_C$ is zero, and there are no discontinuities in the viscosity. This behaviour is equivalent to that of an idealized yield-stress fluid (with a nonlinear viscosity), and would correspond to the observed situation if the fluid were not left to age at all. As $\lambda_0 \to 1$, on the other hand, the threshold $\tau_A$ diverges, which indicates (somewhat unphysically) that the fluid never de-structures. This situation is suggestive of an arbitrarily long period of ageing. Thus, taking different values for $\lambda_0$ between these two limits allows for differing degree of initial ageing: the bigger the value of $\lambda_0$, the longer the ageing time $T_{age}$.

### 2.4. *Relation to previous models*

The forms of the healing and de-structuring terms in (2.3) are similar to those suggested by Barnes (1997), and many authors since. Our form for the viscosity, however, differs from previous models, in which inverse powers or exponentials of $(\lambda_0 - \lambda)$ are more popular. The choice $\lambda_0 = 1$ turns our viscosity in (2.3) into such a function. However, as is clear from the preceding discussion in § 2.3, this choice shifts the viscosity bifurcation at $\tau = \tau_A$ to infinite stress. Hence, to retain a finite, age-dependent threshold for the onset of motion in the analytically convenient fashion outlined in §§ 2.2–2.3, we have adopted (2.3).

Note that our quasi-static thixotropic model requires the choice of a viscosity that yields a finite critical stress $\tau_A$. Earlier models that employ the differential form in (2.2) do not share such a requirement because they predict an exponentially slow convergence of the structure function $\lambda$ to unity; this allows one to incorporate the slow initial ageing of the fluid within the same model as the dynamic structural changes that arise during flow. Here, however, the wide separation of the two characteristic time scales is difficult to incorporate into the shallow-layer framework of § 3 which underlies our theory. Instead, we parameterize the slow initial ageing using $\lambda_0$, and track only the relatively fast viscosity variations during the flow.

## 3. Shallow-flow model

### 3.1. *Dimensional formulation*

As sketched in figure 2, we consider flow over an inclined plane with velocity $\boldsymbol{u} = (u, v, w)$ described by a Cartesian coordinate system $(x, y, z)$, orientated such that the $x$-axis points downslope and the $y$-axis points across the slope. The plane is inclined at an angle $\theta$. The fluid is shallow, with a characteristic depth $H$ that is much smaller than the characteristic length scale for variations over the plane, $L$, so that the aspect ratio is $\varepsilon = H/L \ll 1$. The local fluid depth is $z = h(x, y, t)$.

The flow is incompressible,

$$\frac{\partial u}{\partial x} + \frac{\partial v}{\partial y} + \frac{\partial w}{\partial z} = 0, \tag{3.1}$$

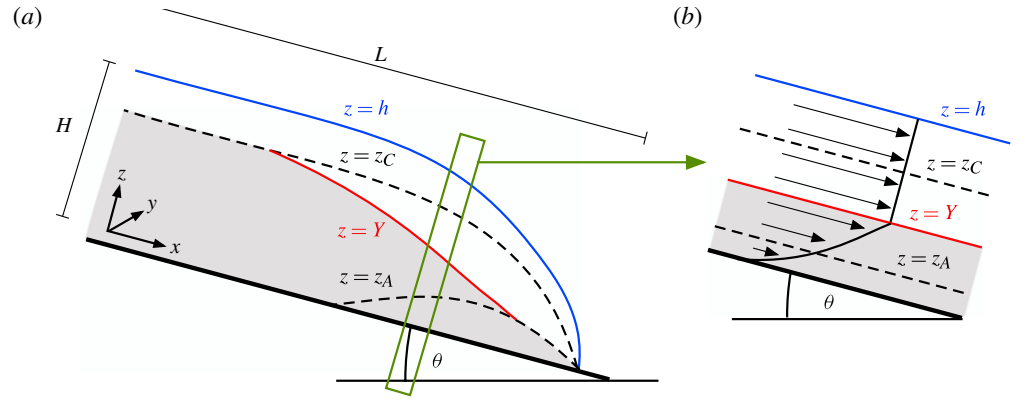


FIGURE 2. (Colour online) A sketch of the flow geometry, showing the coordinate system, the characteristic length and depth, $L$ and $H$, the local fluid depth $h(x, y, t)$, and the curves of the constant critical shear stresses, $z_A = z(\tau_A)$ and $z_C = z(\tau_C)$. The border between structured and de-structured fluid, $z = Z(x, y, t)$, is pieced together from $z = z_A$, $z_C$ and a material section, $z = Y(x, y, t)$; de-structured fluid is shown shaded. ($b$) The profile in $z$ of $u$ through the slice of the flow shown by the rectangle in ($a$).

and satisfies the momentum equations,

$$\rho\left(\frac{\partial \boldsymbol{u}}{\partial t} + \boldsymbol{u}\cdot\boldsymbol{\nabla}\boldsymbol{u}\right) = \rho\tilde{\boldsymbol{g}} - \boldsymbol{\nabla}p + \boldsymbol{\nabla}\cdot\boldsymbol{\tau}, \tag{3.2}$$

where $p$ is the pressure, and $\tilde{\boldsymbol{g}} = (g\sin\theta, 0, -g\cos\theta)$, with constant gravitational acceleration $g$. The deviatoric stresses are related to the rates of strain by (2.1), and the viscosity is set according to (2.3) and (2.4). Just prior to the moment that the fluid is released, the material is fully and uniformly structured, so that $\lambda = \lambda_0$.

The boundary conditions are given by no slip at the base and the stress-free condition at the upper boundary:

$$\boldsymbol{u} = 0 \quad \text{at } z = 0, \qquad \left(\tau_{ij} - p\delta_{ij}\right)n_j = 0 \quad \text{at } z = h(x, y, t), \tag{3.3a,b}$$

where $\delta_{ij}$ is the Kroneker delta and $\boldsymbol{n}$ is the normal to the surface $z = h$. The kinematic condition at the upper boundary is

$$\frac{\partial h}{\partial t} + u\frac{\partial h}{\partial x} + v\frac{\partial h}{\partial y} - w = 0 \quad \text{at } z = h(x, y, t). \tag{3.4}$$

### 3.2. *Dimensionless leading-order formulation*

To remove the dimensions from the equations and pave the way for the shallow-layer theory, we introduce the rescalings

$$t = \frac{L}{U}t^*, \qquad (x, y) = L(x^*, y^*), \qquad (z, h) = H(z^*, h^*), \tag{3.5}$$

$$(u, v) = U(u^*, v^*), \qquad w = \varepsilon U w^*, \qquad p = \rho g H p^*\cos\theta, \qquad \tau_{ij} = \frac{\mu_0 U}{H}\tau^*_{ij}, \tag{3.6}$$

$$\mu = \mu_0\mu^*, \qquad G = TG^*, \qquad \Gamma = \frac{\alpha T U}{H}\Gamma^*, \tag{3.7}$$

where the speed scale

$$U = \frac{H^3 \rho g}{L \mu_0} \cos\theta. \tag{3.8}$$

On discarding the star decoration, and to leading-order in $\varepsilon$, (3.2) reduces to the lubrication equations

$$0 = S - \frac{\partial p}{\partial x} + \frac{\partial \tau_{xz}}{\partial z} = -\frac{\partial p}{\partial y} + \frac{\partial \tau_{yz}}{\partial z} = -1 - \frac{\partial p}{\partial z}, \tag{3.9}$$

where the slope parameter $S = \varepsilon^{-1} \tan\theta$ is assumed to be $O(1)$. The neglect of inertial terms is valid provided that the Reynolds number $Re = \rho UL/\mu_0$ is no larger than $O(\varepsilon^{-1})$. The dimensionless viscosity and structure function can be written as

$$\mu = \frac{\lambda_0}{(\lambda_0 - \lambda)(1 - \lambda)}, \quad G = \frac{(\lambda_0 - \lambda)}{\lambda_0} [1 - \Gamma \tau \lambda (1 - \lambda)] = 0. \tag{3.10a,b}$$

The dominant components of the rate-of-strain tensor are $\dot\gamma_{xz} = \partial u/\partial z + O(\varepsilon^2)$ and $\dot\gamma_{yz} = \partial v/\partial z + O(\varepsilon^2)$. Therefore, to leading-order, the stress conditions in (3.3*b*) become

$$p = \mathrm{d}u/\mathrm{d}z = \mathrm{d}v/\mathrm{d}z = 0 \quad \text{at } z = h(x, y, t). \tag{3.11}$$

The kinematic condition (3.4) is unchanged after scaling.

Equations (3.9) and (3.11) imply that the pressure is hydrostatic,

$$p = h - z, \tag{3.12}$$

and the shear stresses are given by $(\tau_{xz}, \tau_{yz}) = (h - z)(S - \partial h/\partial x, -\partial h/\partial y)$, so $\tau = \sqrt{\tau_{xz}^2 + \tau_{yz}^2} = (h - z)\mathscr{T}$, with $\mathscr{T} = \sqrt{(S - \partial h/\partial x)^2 + (\partial h/\partial y)^2}$.

### 3.3. *Anatomy of the flow*

The rheological model in (3.10) implies that, at each position $(x, y)$ on the inclined plane, changes in fluid structure occur when the local stress invariant $\tau \equiv (h - z)\mathscr{T}$ becomes equal to one of the critical values, $\tau_C$ and $\tau_A$. The stress contours $\tau = \tau_C$ and $\tau = \tau_A$ therefore define two surfaces, $z = z_C \equiv h - \tau_C/\mathscr{T}$ and $z = z_A \equiv h - \tau_A/\mathscr{T}$. Above $z = z_C$, the stress is less than $\tau_C$, indicating that the fluid is structured with $\lambda = \lambda_0$ and $\dot\gamma = 0$. That is, the flow is plug-like with $\partial u/\partial z = \partial v/\partial z = 0$. On the other hand, below $z = z_A$, the stress is greater than $\tau_A$, and the fluid is de-structured with $\lambda = \lambda_-$, indicating that there is vertical shear, $\dot\gamma > 0$ (see figure 2).

Between the two stress surfaces, $z_C < z < z_A$, the structural state of the fluid depends on the stress history of each fluid element. Initially, the fluid is prepared in the fully structured state with $\lambda = \lambda_0$ everywhere. Therefore, when the fluid is released, the de-structured fluid will be exactly bounded above by $z = z_A$. During the ensuing flow, if the stress increases locally this surface may migrate upwards into structured fluid and de-structure that material. However, the runout of the fluid can also reduce the local stress, demanding that the surface $z = z_A$ descend through the fluid, leaving behind de-structured fluid. Those fluid elements move with the flow and only re-structure when the local stress falls below $\tau_C$ along the level $z = z_C$.

Thus, the interface, or yield surface, $z = Z(x, y, t)$ which separates de-structured fluid below from fully structured fluid above, must consist of three different segments (see figure 2). First, there is a de-structuring front $Z \equiv z_A$ wherever the surface $z = z_A$ is ascending into currently structured fluid. Second, there is a re-structuring front $Z \equiv z_C$

whenever the surface $z = z_C$ is descending into currently de-structured fluid. Third, in between these fronts the yield surface corresponds to the border of material that was initially de-structured by an increase in local stress, but was then left behind as the stress decreased; this piece of the yield surface is necessarily a material curve, $Z \equiv Y(x, y, t)$, which satisfies the kinematic condition,

$$\frac{\partial Y}{\partial t} + u\frac{\partial Y}{\partial x} + v\frac{\partial Y}{\partial y} - w = 0 \quad \text{on } z = Y(x, y, t). \tag{3.13}$$

### 3.4. *Synopsis of the model*

To summarize, the local fluid depth evolves according to (3.4), or, using the integral of (3.1),

$$\frac{\partial h}{\partial t} + \frac{\partial}{\partial x}\int_0^Z (h - z)\,\frac{\partial u}{\partial z}\,\mathrm{d}z + \frac{\partial}{\partial y}\int_0^Z (h - z)\,\frac{\partial v}{\partial z}\,\mathrm{d}z = 0 \tag{3.14}$$

where $z = Z(x, y, t)$ is the yield surface that divides fully structured fluid above from de-structured fluid below. The fully structured fluid in $Z < z < h$ flows in a plug-like fashion with $\lambda = \lambda_0$ and $\partial u/\partial z = \partial v/\partial z = 0$. The underlying de-structured material has a spreading velocity that is dictated by integrating

$$\mu\frac{\partial u}{\partial z} = \left(S - \frac{\partial h}{\partial x}\right)(h - z) \equiv \tau_{xz} \quad \text{and} \quad \mu\frac{\partial v}{\partial z} = -\frac{\partial h}{\partial y}(h - z) \equiv \tau_{yz}, \tag{3.15a,b}$$

where

$$\mu(\lambda) = \frac{\lambda_0}{(1 - \lambda)(\lambda_0 - \lambda)}, \quad \lambda = \lambda_- = \frac{1}{2}\left[1 - \left(1 - \frac{4}{\Gamma\tau}\right)^{1/2}\right], \tag{3.16a,b}$$

and

$$\tau = \sqrt{\tau_{xz}^2 + \tau_{yz}^2} = \mathscr{T}(h - z), \quad \mathscr{T} = \sqrt{\left(S - \frac{\partial h}{\partial x}\right)^2 + \left(\frac{\partial h}{\partial y}\right)^2}. \tag{3.17a,b}$$

The yield surface $z = Z(x, y, t)$ matches $z = z_A \equiv h - \tau_A/\mathscr{T}$ if that curve is moving into structured fluid, or $z = z_C \equiv h - \tau_C/\mathscr{T}$ if this surface is moving into de-structured fluid. Otherwise, the yield surface evolves as a material curve as in (3.13); equivalently,

$$\frac{\partial Y}{\partial t} + \frac{\partial}{\partial x}\int_0^Y (Y - z)\,\frac{\partial u}{\partial z}\,\mathrm{d}z + \frac{\partial}{\partial y}\int_0^Y (Y - z)\,\frac{\partial v}{\partial z}\,\mathrm{d}z = 0. \tag{3.18}$$

We solve (3.14)–(3.18) numerically, in both two and three dimensions, using second-order centred finite differences in space, and a second-order midpoint method in time. We place a thin pre-wetting fluid film (of thickness $h = 10^{-3}$) on the substrate to avoid any difficulties with a moving contact line. The flux terms in (3.14) and (3.18) can be evaluated analytically to expedite the computations (the expressions for these integrals are rather convoluted and not very informative, so we avoid quoting them). Calculating the location of the yield surface $z = Z(x, y, t)$ is complicated by the fact that we do not know, *per se*, where the material part $Z = Y$ joins the stress contours $Z = z_A$ and $Z = z_C$. Initially, the yield surface is equal to the stress contour $Z = z_A$, as the fluid is fully structured with $\lambda = \lambda_0$ prior to its release. At subsequent times, we calculate the yield surface by first solving (3.18) numerically to evolve every fluid element on

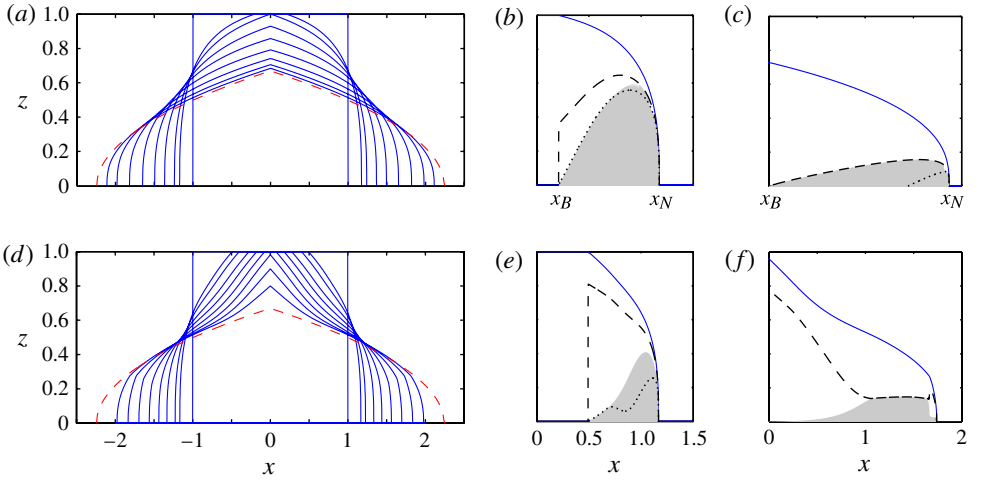


FIGURE 3. (Colour online) Planar slumps on a horizontal plane ($S = 0$) for (*a–c*) $\lambda_0 = 0.8$ and (*d–f*) $\lambda_0 = 0.95$, with $\Gamma = 40$ ($\tau_C = 0.1$): (*a*) and (*d*) snapshots of the free surface $z = h$ at times $t = 0, 1/2, 1, 2, 4, 8, 16, 32$, and 64, together with the final rest state (dashed) from (4.2); (*b,c,e,f*) $z = h$ (solid), $z = z_C$ (dashed), and $z = z_A$ (dotted) in $x > 0$ at times: (*b,e*) $t = 1/2$; and (*c,f*) $t = 20$. De-structured fluid is shown shaded. The position of the nose $x_N$ and the back $x_B$ of the flowing current are marked in (*b*) and (*c*). In (*c*), the material part of the yield surface $z = Y$ is very short, and $Z = z_C$ over most of the fluid. In (*f*), $z = z_A$ is positive only very close to the moving front.

the current yield surface at the points of the computational grid. We then update the critical stress contours $z_A$ and $z_C$, and select $Z = Y$ if $z_A \leqslant Y \leqslant z_C$, $Z = z_A$ if $Y < z_A$, and $Z = z_C$ if $z_C < Y$.

The characteristic length scales of the flow $L$ and $H$ can be used to scale out two of the free parameters of the problem. For all the results presented here, we fix the total volume of fluid $V = 2$ and the initial height of the fluid $h(t = 0) = 1$. We are then left with three free parameters: the slope $S$, the structure parameter $\lambda_0$, and $\Gamma$, which sets the critical stresses $\tau_C$ and $\tau_A$.

## 4. Numerical results

### 4.1. *Two-dimensional slumps on a horizontal plane*

We begin by considering the planar slumping on a horizontal plane ($S = 0$) of a rectangular block of fluid with initial profile, $h(x, 0) = 1$ for $-1 \leqslant x \leqslant 1$ and $h(x, 0) = 0$ for $|x| > 1$. Figure 3 shows snapshots of numerical solutions for two values of $\lambda_0$, and $\Gamma = 40$. For the case with less initial structure ($\lambda_0 = 0.8$; figure 3*a–c*), the fluid slumps much like an idealized yield-stress fluid (e.g. Balmforth *et al.* 2006*b*), and, except at early times, the yield surface $z = Z$ lies mostly along the stress contour $z = z_C$. For greater initial structure ($\lambda_0 = 0.95$; figure 3*d–f*), the nose of the current advances in a similar fashion to the lower value of $\lambda_0$. However, the raised interior of the flow collapses much more slowly because the fluid only de-structures over a relatively thin basal region, owing to the fact that the stress over most of the fluid has never exceeded $\tau_A$.

We define $x_N(t)$ as the position of the right-hand nose of the current, and $x_B(t)$ as the location of the rear of the moving section of fluid in $x > 0$ (i.e. the least positive

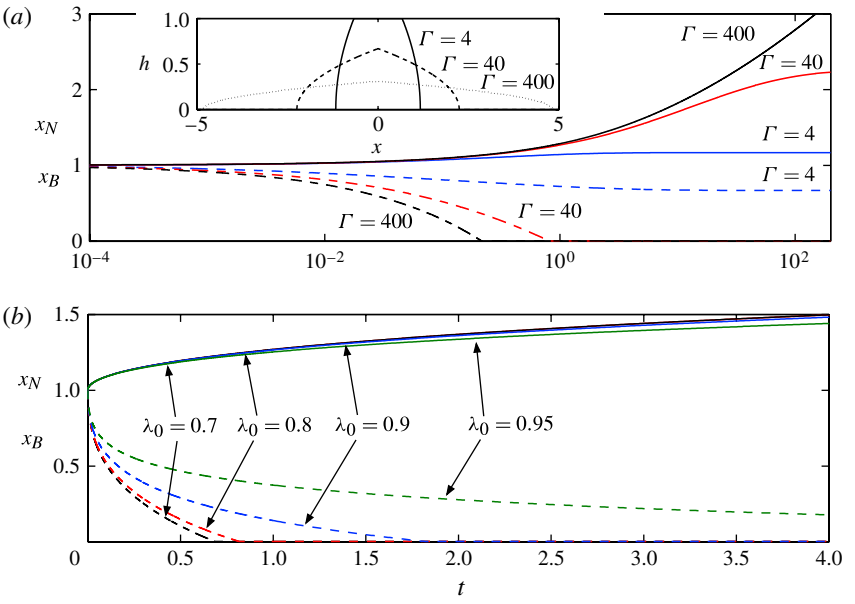


FIGURE 4. (Colour online) Time series of $x_N(t)$ (solid) and $x_B(t)$ (dashed) for planar slumps on a horizontal plane ($S = 0$). (*a*) Results for the values of $\Gamma$ indicated, at fixed initial structure $\lambda_0 = 0.8$; the inset shows the final states given by (4.2) and (4.3). (*b*) Results for the values of $\lambda_0$ indicated, at fixed $\Gamma = 40$.

value of $x$ for which $h < 1$; the 'back' of the current; see figure 3). In view of the initial condition, $x_N(0) = x_B(0) = 1$, and all the fluid is in motion once $x_B$ decreases to 0. Figure 4 plots time series of $x_N(t)$ and $x_B(t)$ for the two solutions shown earlier in figure 3, along with other solutions for different values of $\Gamma$ and ageing times. For small $\Gamma$, $\tau_A$ and $\tau_C$ are large and the fluid does not slump very far, coming to rest before $x_B$ reaches the origin. With higher $\Gamma$, more fluid de-structures and the slump flows further. The degree of ageing ($\lambda_0$) exerts little influence on the advance of the nose of the current because the stress is always increased sufficiently to exceed $\tau_A$ by steepening the slope there. However, $x_B(t)$ retreats increasingly slowly as $\lambda_0$ increases, in agreement with the results in figure 3.

In all cases, the slump finally comes to rest when all the material has fully re-structured. This arises when the stress falls below $\tau_C$ everywhere, which, from (3.15) with $z = S = \tau_{yz} = 0$, demands that

$$\left| h \frac{\partial h}{\partial x} \right| \leqslant \tau_C = \frac{4}{\Gamma}. \tag{4.1}$$

If $\Gamma < 12$, the yield stress $\tau_C$ is large enough that $x_B$ never reaches $x = 0$, and a central section of fluid remains immobile with $h = 1$; elsewhere, the equality in (4.1) is attained. Hence,

$$h(x) = \begin{cases} 1 & \text{if} \quad |x| < X_1, \\ \left[1 - 8\Gamma^{-1}\left(|x| - X\right)\right]^{1/2} & \text{if} \quad |x| \geqslant X_1; \end{cases} \qquad X_1 = 1 - \tfrac{1}{12}\Gamma. \tag{4.2}$$

If, instead, $\Gamma > 12$, then the fluid fully slumps; the equality in (4.1) applies throughout and

$$h(x) = \left[\frac{8}{\Gamma}\,(X_2 - |x|)\right]^{1/2}; \quad X_2 = \left(\frac{9\Gamma}{32}\right)^{1/3}. \tag{4.3}$$

The final states predicted by (4.2)–(4.3) are included in figures 3 and 4, and are identical to those obtained for an idealized yield-stress fluid with yield stress $\tau_C$ (see e.g. Balmforth *et al.* 2006*a*). Although the final slumped states do not depend on the initial structure $\lambda_0$, the numerical results in figure 4 emphasize how the approach to the final state becomes increasingly long as $\lambda_0$ increases towards 1.

The numerical solutions in figure 3 expose a crucial hidden detail of the theoretical model. It is evident from the snapshots of $h(x, t)$ that fluid spreads out from the midline of the slumping current at $x = 0$. This spreading is mediated by the de-structured lower layer of the fluid, which conveys along the overlying structured fluid. Importantly, even though the structured fluid flow is plug-like in the vertical ($\partial u/\partial z = 0$), this material still undergoes a much weaker horizontal extension. In other words, the structured fluid is not rigid, despite the infinite viscosity suggested by (3.10). This inconsistency is equivalent to the lubrication paradox of a yield-stress fluid (Balmforth & Craster 1999) and is resolved as follows: the shallow-flow approximation of § 3 amounts to the leading-order of an asymptotic expansion. Implicitly, it assumes that the viscosity of the structured fluid is sufficiently large that it suppresses the vertical shear. However, the viscosity is not taken to be so large that the extensional stresses, $\tau_{xx}$ and $\tau_{zz} \equiv -\tau_{zz}$, become promoted into the leading-order balance of forces in (3.9). In other words, our structured fluid does not have an infinite viscosity, merely one that is large; in our asymptotic scheme, the underlying assumption is that $1 \ll \mu(\lambda_0) \ll \varepsilon^{-1}$. Consequently, the enhanced viscosity of the structured fluid only suppresses the vertical shear, not the horizontal extension. We return to this important point later in § 5.2.2; for now, we note only that this detail is a feature of all the numerical solutions presented in § 4.

### 4.2. *Two-dimensional slumps on an inclined plane*

#### 4.2.1. *Results*

Motivated by our experiments in § 5, we initiate planar, inclined slumps ($S > 0$) by taking the initial height profile to be given by the final rest state of a slumped dome on a horizontal plane. That is, $h(x, 0)$ is set by either (4.2) or (4.3), depending on the value of $\Gamma$. In order to avoid discontinuities in the stress, the initial profile is smoothed at points where the free surface has a discontinuous derivative (i.e. for $\Gamma > 12$, the height is smoothed at $x = 0$). Figure 5(*b–f*) shows numerical results for three different ageing times, with $\Gamma = 40$ ($\tau_C = 4/\Gamma = 0.1$) and $S = 1$. For comparison, figure 5(*a*) shows a solution for a Bingham fluid (cf. Balmforth *et al.* 2006*b*) with the same yield stress $\tau_C$. The height profile of the Bingham current increases from the back, where the fluid remains stationary, to a maximum just behind the front. The thixotropic case with smaller ageing time ($\lambda_0 = 0.8$; figure 5*b,e*) shows broadly similar features. For longer ageing ($\lambda_0 = 0.9$ and 0.95; figure 5*c,d,f*), however, the current leaves behind a striking raised remnant of structured fluid, and develops a pronounced nose at the front, much as observed in the computations reported by Coussot *et al.* (2005), albeit for a different rheological model. Both features result because the stress on the fluid is greatest below the highest point of the initial profile; the most significant de-structuring thus occurs at the centre of the current.

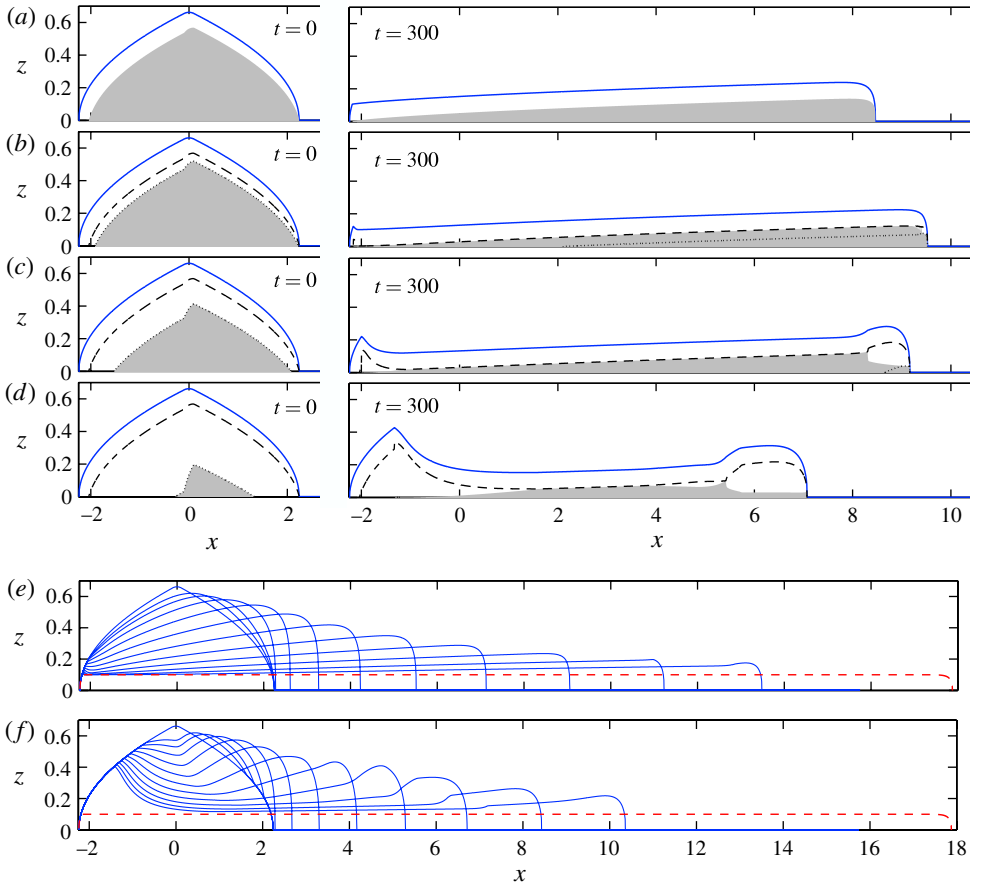


FIGURE 5. (Colour online) Inclined planar slumps for $S = 1$ and $\Gamma = 40$ ($\tau_C = 0.1$). Shown are the height $z = h$ (solid), and the stress contours $z = z_C$ (dashed) and $z = z_A$ (dotted); de-structured fluid is shown shaded. (*a–d*) Profiles at $t = 0$ (left) and $t = 300$, for: (*a*) a Bingham fluid with yield stress $\tau_C = 0.1$; (*b*) thixotropic fluid with $\lambda_0 = 0.8$; (*c*) $\lambda_0 = 0.9$; (*d*) $\lambda_0 = 0.95$. Initially, $z(\tau_A) = Z$, and at $t = 300$ in (*c,d*), $z(\tau_A)$ is mostly negative. (*e,f*) Snapshots of the height $z = h$ at $t = 0$, 10, 20, 40, 80, 160, 320 and 640, for (*e*) $\lambda_0 = 0.8$, and (*f*) $\lambda_0 = 0.95$; the final states, given by (4.7), are shown by the dashed line.

Time series of the position of the nose of the current $x_N(t)$ for a suite of computations at fixed $\Gamma = 40$ are shown in figure 6. For small values of $\lambda_0$, the current travels faster than the corresponding Bingham fluid because the de-structured thixotropic material has a smaller, rate-dependent viscosity. The currents of older fluid (larger $\lambda_0$) are slower, however, and are characterized by an increasingly long delay at the beginning before the nose of the current starts to move; both effects arise because less fluid in the current is de-structured and able to flow (see below). Moreover, if $\lambda_0$ is too large, the fluid never moves at all; this points to an age-dependent critical slope that must be exceeded in order for the fluid to collapse (compare the solutions for $S = 0.8$ and $S = 1$ in figures 6*a* and 6*b*). The critical slope is discussed further in § 4.2.2.

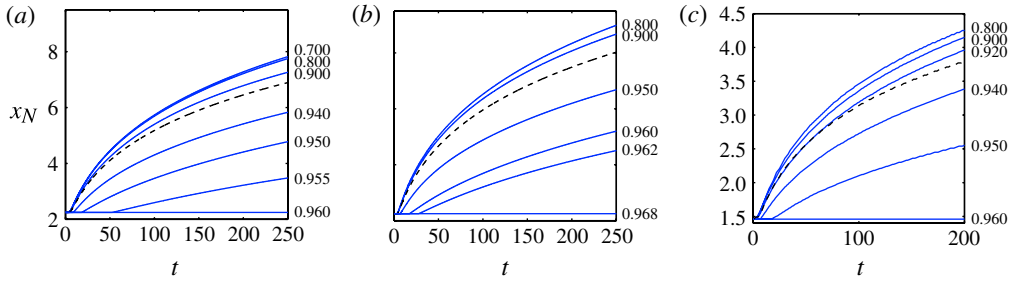


FIGURE 6. (Colour online) Position of the nose $x_N(t)$ with $\Gamma = 40$, for different values of the initial structure $\lambda_0$ as indicated on the right-hand side of each panel: (*a*) two-dimensional slump with $S = 0.8$; (*b*) two-dimensional slump with $S = 1$; (*c*) three-dimensional slump with $S = 1$. The dashed lines show the results for a Bingham fluid with yield stress $\tau_C = 0.1$. For the largest value of $\lambda_0$ in each subfigure, the slope is below the critical angle, and the current remains stationary.

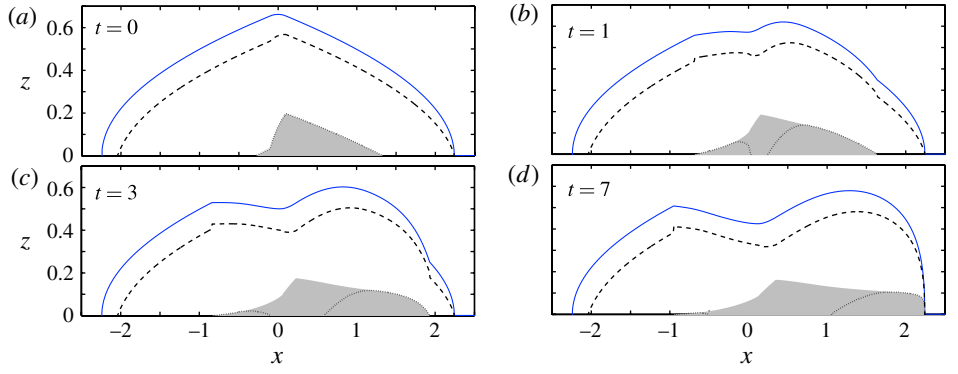


FIGURE 7. (Colour online) Four snapshots of the current in figure 5(*f*) ($\Gamma = 40$, $S = 1$, $\lambda_0 = 0.95$), at the times indicated. Shown are the height $z = h$ (solid) and the two stress contours $z = z_C$ (dashed), $z = z_A$ (dotted); de-structured fluid is shaded.

The initial delay in the advance of the nose arises because, at angles just above the critical value, the fluid only de-structures in the centre of the current. The dynamics are shown in more detail in figure 7, which displays the early-time evolution of the current of figure 5(*f*) with $\lambda_0 = 0.95$. At $t = 0$, the stress contour $z = z_A$ is confined to the core of the initial dome. Once the material is released, this contour propagates down the incline (and slightly upslope) due to the steepening of the local free surface, de-structuring fluid closer to the dome's edge. Simultaneously, the stress falls over the collapsing centre of the dome, and the stress contour $z = z_A$ descends through the fluid leaving behind de-structured fluid and a material yield surface. The nose of the current remains stationary until it is reached by the advancing contour $z = z_A$, which, for this example, occurs at $t \approx 7$ (figure 7*d*).

Results for stronger critical stresses ($\Gamma = 4$; $\tau_C = 1$) are shown in figure 8. The initial condition now has a flat central section, as given by (4.2). Nevertheless, the evolution of the current for different values of $\lambda_0$ is similar to the previous results with $\Gamma = 40$ (figure 5). One notable difference in figure 8 is the development of

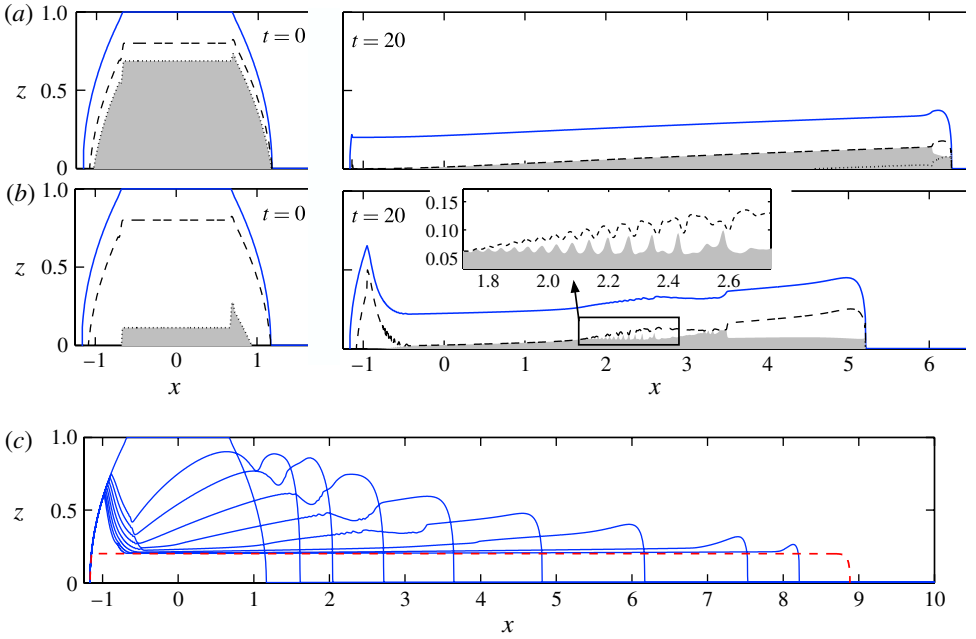


FIGURE 8. (Colour online) Inclined planar slumps for $S = 5$ and $\Gamma = 4$ ($\tau_C = 1$), at times $t = 0$ and $t = 20$, showing $z = h$ (solid), the two stress contours $z = z_C$ (dashed), $z = z_A$ (dotted), and de-structured fluid (shaded), for (*a*) $\lambda_0 = 0.8$ and (*b*) $\lambda_0 = 0.94$. The inset to (*b*) shows a magnification of the waves on the material yield surface. (*c*) Snapshots of $h$ for $\lambda_0 = 0.94$, at times $t = 0, 1, 2, 4, 8, 16, 32, 64, 128$, together with the final rest state given by (4.7) (dashed).

spatial structure on the surfaces $z = h$ and $z = Y$, which is most prominent for larger $\lambda_0$ (figure 8*b*). We have also observed similar structure in computations with other parameter settings. The structure typically takes the form of short-wavelength travelling waves on the material yield surface $z = Y$. The waves often appear when sharp horizontal gradients arise in the stress and can pose a problem with spatial resolution when the wavelength becomes too short. Both the height of the free surface and the global features of the flow remain largely unaffected by these waves, which move along the material yield surface and are damped at intersections with the critical stress contours $z = z_C$ or $z = z_A$. In the Appendix, we rationalize these waves in terms of an interfacial instability.

4.2.2. *The critical slope*

If the stress on the fluid layer does not exceed $\tau_A$ anywhere, the fluid remains fully structured and cannot flow. The situation corresponds to a critical slope $S_c$, which can be calculated analytically. When the initial dome, whose profile satisfies $|h\partial h/\partial x| = \tau_C = 4/\Gamma$ (4.1), is placed on a slope $S$, the stress along the base of the current becomes

$$\tau = \left| S - \frac{\partial h}{\partial x} \right| h = \left| Sh - \tau_C \mathrm{sgn}\left( \frac{\partial h}{\partial x} \right) \right|. \tag{4.4}$$

The fluid will not de-structure if $\tau < \tau_A = [\Gamma\lambda_0(1-\lambda_0)]^{-1}$. It follows, on using (4.2) and (4.3), that the critical slope $S_c$ is

$$S_c \equiv \frac{\tau_A - \tau_C}{\max(h)} = \frac{(1-2\lambda_0)^2}{\Phi\lambda_0\,(1-\lambda_0)} \quad \text{where } \Phi = \begin{cases} \left(12\Gamma^2\right)^{1/3}, & \Gamma > 12, \\ \Gamma, & \Gamma \leqslant 12. \end{cases} \tag{4.5}$$

When the fluid is not aged, $T_{age} = 0$ and $\lambda_0 = 1/2$, which implies $S_c = 0$. The fluid therefore flows at any non-zero angle, reflecting how the slumped dome used as the initial condition is already held at its yield stress with $\tau = \tau_A$ everywhere. The addition of any degree of slope unavoidably raises $\tau$ on the downward face of the dome, thereby initiating collapse (an imitation of the behaviour of a yield-stress fluid). As the ageing time, and thus $\lambda_0$, increases, there is an increased separation between the two stresses $\tau_C$ and $\tau_A$, and the critical slope $S_c$ increases. As $\lambda_0 \to 1$, $S_c \to \infty$, in which limit the shallow-layer framework of the model breaks down.

4.2.3. *Final rest state*

As for the slump on a horizontal plate (§ 4.1), the final state for an inclined current is again given by the height profile for which the stress on the base has fallen below $\tau_C$ everywhere, implying that the fluid fully re-structures. Such states are identical to those for a Bingham fluid with a yield stress $\tau_C = 4/\Gamma$ (see e.g. Balmforth *et al.* 2006*b*), and are given by

$$\left| S - \frac{\partial h}{\partial x} \right| h \leqslant \tau_C. \tag{4.6}$$

At the back of the current, the fluid never slumps because the basal stress on the left of (4.6) never exceeds $\tau_C$. The slumped forward section, on the other hand, has a basal stress that approaches $\tau_C$; (4.6) then provides the implicit solution

$$\log\left(1 - \frac{S}{\tau_C}h\right) + \frac{S}{\tau_C}h = \frac{S^2}{\tau_C}\,(x - x_F)\,, \tag{4.7}$$

where $x_F$ is a constant of integration corresponding to the final position of the nose of the current; this constant is determined by matching (4.7) with the unslumped initial condition at the back of the current in such a way as to obtain the correct fluid volume.

Final profiles from (4.7) are shown in figures 5(*e*,*f*) and 8(*c*). The profiles are almost flat, with a steep drop at the nose, and are independent of the ageing time $T_{age}$ (i.e. $\lambda_0$), provided the inclination angle is greater than the critical slope $S_c$. The raised structured remnant at the back of the current for higher $\lambda_0$ must therefore eventually disappear; the numerical results indicate that this late stage of the evolution is much slower than the initial spreading of the current.

### 4.3. *Three-dimensional slumps on an inclined plane*

As for the planar slumps, our initial condition for three-dimensional currents on an incline is given by the profile of a slumped dome on a horizontal surface. That profile is axisymmetric and, for $V = 2$, is given by

$$h(x, y, t = 0) = \left[\frac{8}{\Gamma}\left(R - \sqrt{x^2 + y^2}\right)\right]^{1/2}; \quad R = \left(\frac{15}{8\pi}\right)^{2/5}\left(\frac{\Gamma}{2}\right)^{1/5}, \tag{4.8}$$

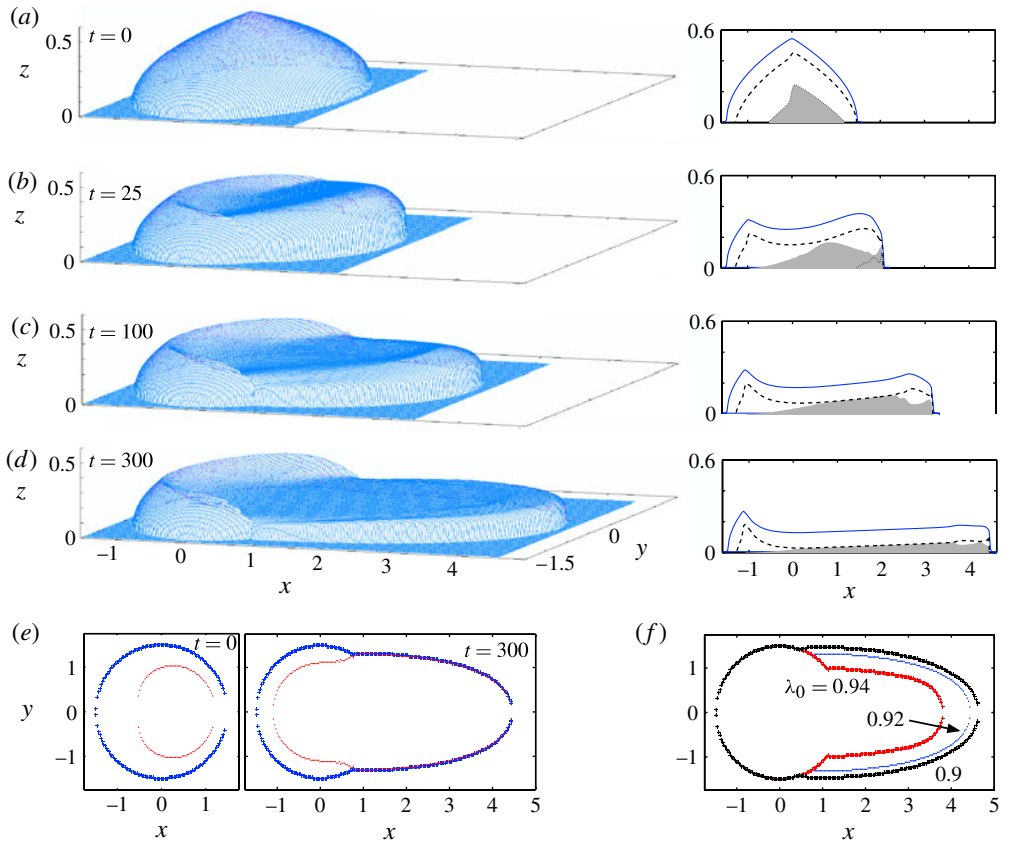


FIGURE 9. (Colour online) Three-dimensional slump on an incline with slope $S = 1$, $\lambda_0 = 0.92$ and $\Gamma = 40$. (*a–d*) $z = h(x, y, t)$ as a surface above the $(x, y)$-plane at the times indicated (left), together with the midsection ($y = 0$) profiles of $h$ (solid), $z_C$ (dashed), and $z_A$ (dotted) (right). De-structured fluid is shown shaded. (*e*) The edge of the current (stars) and the border of unslumped structured fluid (dots) at $t = 0$ and 300. (*f*) A comparison of the edge of the current at $t = 300$ for $\lambda_0 = 0.9$, 0.92, and 0.94 ($\Gamma = 40$, $S = 1$).

provided that $\Gamma > \sqrt{240/\pi} \approx 8.7$, which corresponds to the parameter setting used below. If $\Gamma < \sqrt{240/\pi}$, the fluid does not fully slump on a horizontal plane and the initial condition has a flat top analogous to the two-dimensional profile in (4.2).

Figure 9(*a–e*) shows a numerical solution for $\Gamma = 40$, $S = 1$, and $\lambda_0 = 0.92$. As for the planar slumps, a remnant of structured fluid is left behind at the back of the current. The remnant corresponds to the least stressed part of the initial dome, where $\tau < \tau_A$, and is similar to the 'horseshoe' observed experimentally by Coussot *et al.* (2002*a*). As shown in figure 9(*f*), the extent of the structured horseshoe increases with $\lambda_0$, or equivalently with the ageing time.

The height profile and stress curves over the midsection ($y = 0$) of the three-dimensional slump in figure 9(*a–d*) are qualitatively similar to those of planar currents with large $\lambda_0$ (cf. figure 5*c–d*). In particular, once again fluid yields only at the core of the initial dome and it takes a finite length of time for the yield surface to advance through the fluid to the nose of the current (see also figure 5*e*). The delayed progress

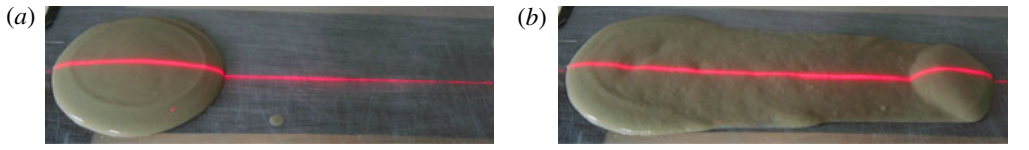


FIGURE 10. (Colour online) Snapshots of an experiment with 10 % by volume bentonite solution, $T_{age} = 240$ min, and an angle of 20°: (*a*) after $t = 5$ s; (*b*) after $t = 50$ s. The initial diameter of the fluid is ∼13 cm

of the nose of three-dimensional currents with different degrees of initial structure $\lambda_0$ is comparable with the results for planar slumps, as shown in figure 6(c).

As in two dimensions, there is an age-dependent critical angle below which the initial profile does not collapse. Similarly the final rest state of the current can be calculated by matching the unslumped part of the deposit (with a profile set by the initial condition) to the solution of

$$\left(S + \frac{\partial h}{\partial x}\right)^2 + \left(\frac{\partial h}{\partial y}\right)^2 = \frac{\tau_C^2}{h^2}, \tag{4.9}$$

corresponding to equating the basal shear stress with $\tau_C$ (cf. Balmforth *et al.* 2002). As in the planar case discussed in § 4.2.3, this final state has no raised remnant at its back. The horseshoe must therefore be slowly eroded away over a much longer time scale than the initial rate of spreading.

## 5. Experiments

### 5.1. *The setup*

We carried out a series of experiments on an inclined plane to compare with the predictions of our model. The experimental setup consisted of a 1 $m^2$ glass plate, which was hinged at one end, and could be tilted and held at a desired angle using a pulley system. As a model thixotropic fluid, we used a suspension of bentonite clay in filtered water (10 % by volume, *Quik-Gel* sodium bentonite, *Baroid drilling fluids*). We also carried out experiments with tomato ketchup (Heinz), which are discussed very briefly in § 5.3. In preparation for each experiment, the bentonite solution was vigorously stirred for twenty minutes to homogenize the fluid and destroy its internal structure. A fixed volume (150 ml) of the material was then poured into a hollow cylindrical (5 cm radius) mould set upon a horizontal Plexiglas sheet whose surface had been roughened by sandpaper. Quickly raising the mould allowed the sample to slump to rest, creating a dome equivalent to the initial conditions used for the theoretical computations. The slumped dome was then left to age for a time $T_{age}$ under an airtight cover to limit evaporation. Finally, the roughened Plexiglas and its dome were fixed onto the glass plate, which was then tilted to a desired angle. The surface of the current along its midsection was recorded using a laser line projected onto the fluid surface from directly above (figure 10). The roughening of the Plexiglas sheet was essential to eliminate any macroscopic slip at the base of the current, which is known to affect bentonite solutions (e.g. Coussot *et al.* 2002*b*).

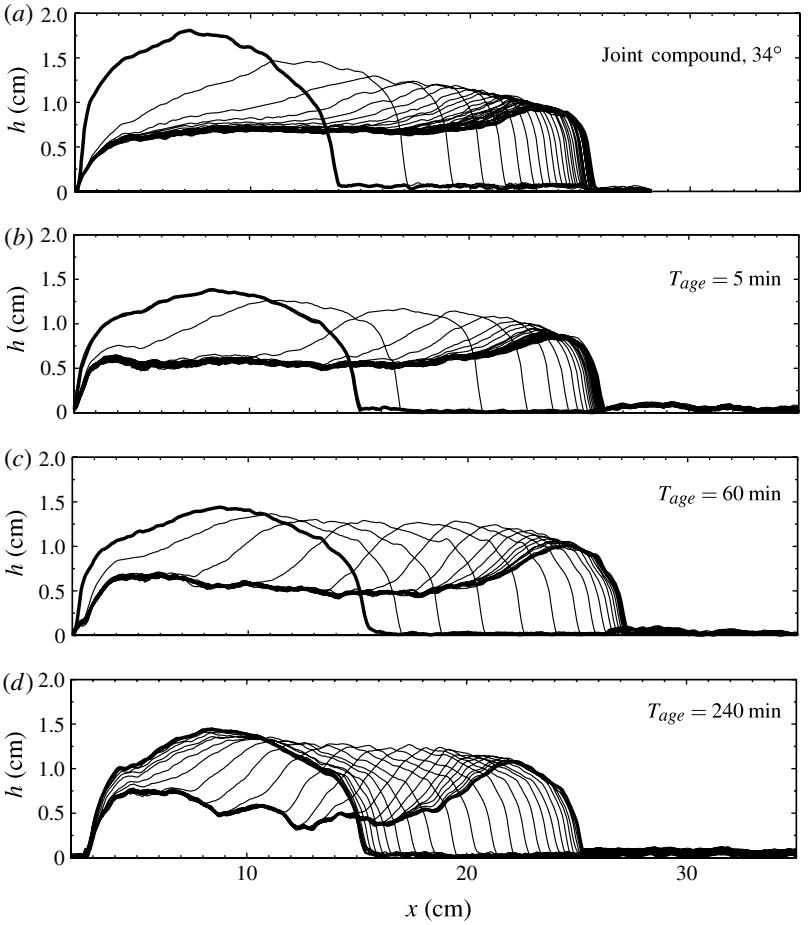


FIGURE 11. Experimental height profiles along the midsection of currents of joint compound and bentonite. The joint compound, shown in (*a*), flows down a 34° slope. The bentonite, shown in (*b*)–(*d*), is on a 20° slope and the ageing times $T_{age}$ are indicated. The profiles are plotted every 2 s, except those in (*b*), which are 0.5 s apart. Bold lines signify the initial and final profiles.

## 5.2. *Bentonite*

### 5.2.1. *Results*

Measurements of the surface profiles of flowing currents of bentonite clay are shown in figures 11 and 12. Figure 11 shows profiles of samples with different ageing times $T_{age}$ on inclines of 20°; figure 12 shows profiles on slightly steeper inclines of 24°. As a comparison, we carried out some experiments with a 'joint compound' solution (*Sheetrock* all-purpose joint compound), which, over the time scale of an experiment, appeared similar to an ideal yield-stress fluid. Measurements of the height of the joint compound are shown in figure 11(*a*).

The measurements confirm that the behaviour of bentonite is strongly dependent on the ageing time. Consider, for example, the results on a 20° slope (figure 11*b–d*). For very small ageing times, the behaviour is similar to that of the joint compound (figure 11*a*): the fluid evolves rapidly after the experiment starts and primarily slumps

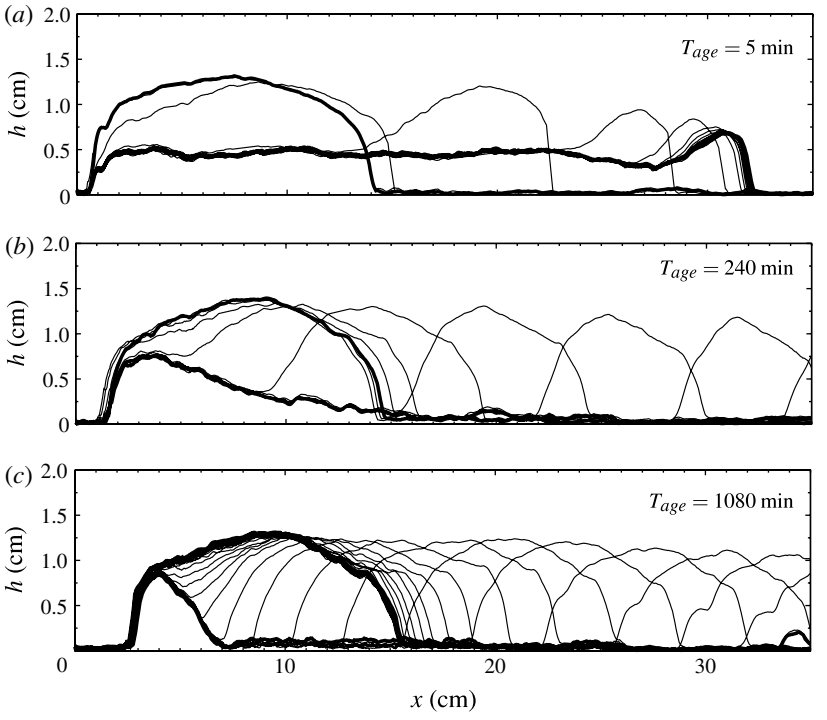


FIGURE 12. Experimental height profiles along the midsection of bentonite currents on a 24° slope, for the ageing times $T_{age}$ indicated. Profiles are plotted every 2 s, except those in (*a*), which are 0.5 s apart. Bold lines signify the initial and final profiles. In (*b,c*), the current flows off the end of the plate.

forwards, piling material up towards the front (the slight residual bump near the front of the fluid is not consistent with the theoretical results for a yield-stress fluid, and is perhaps the result of surface tension effects or a different fluid rheology). However, as the ageing time $T_{age}$ increases, the samples behave quite differently: the current thins most dramatically in the middle, a horseshoe-shaped remnant is left behind at the back of the current, and a raised nose detaches at the front. These features are even more striking on a slope of 24° (figure 12). Note that, even in the most extreme examples, there was always a thin lubricating layer of de-structured fluid left coating the plane, and the nose did not appear to be suffering macroscopic slip over the Plexiglas (which did occur when that surface was not roughened; the slipping current left almost no fluid trailing behind).

Figure 13(*a,b*) shows time series of the position of the nose of the current $x_N(t)$ for two different angles and a variety of ageing times $T_{age}$. These plots illustrate how, for small $T_{age}$, the current accelerates quickly at small times. However, as $T_{age}$ increases, there is an increasingly long delay before motion begins, and then, once underway, accelerations are more gradual. Figure 13(*a,b*) also highlights how the current comes to an abrupt halt after flowing down the plane.

Figure 13(*c*) shows the final position of the nose of the current, $x_F$, as a function of the inclination angle, for six different ageing times $T_{age}$. A first conclusion that can be drawn from these results is that, if the inclination is below a critical angle that depends on the ageing time, the fluid does not move at all. Second, for small values

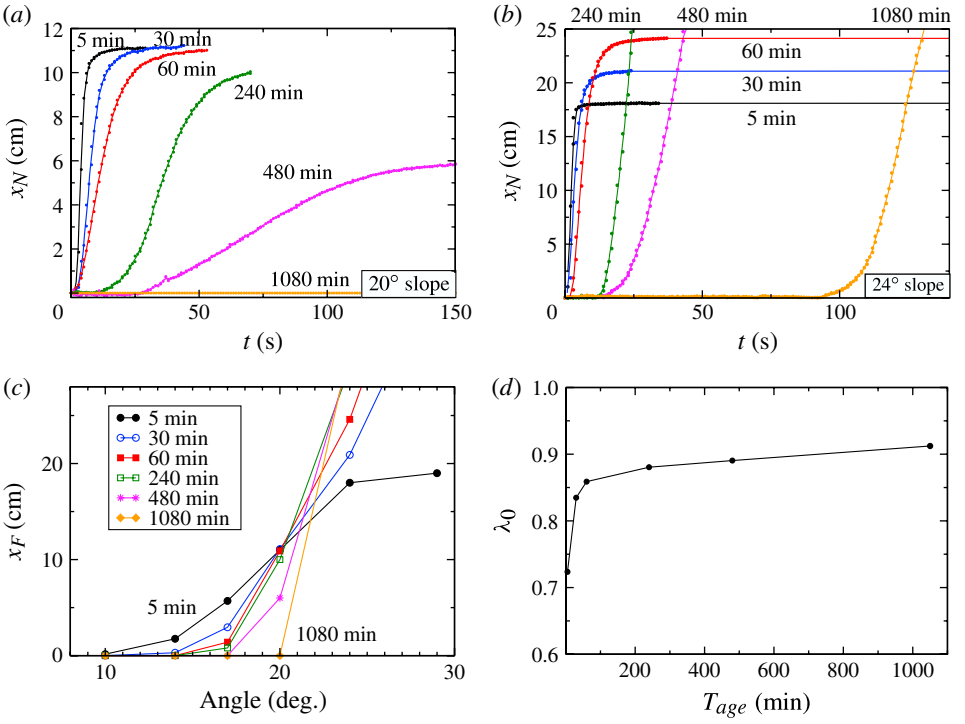


FIGURE 13. (Colour online) (*a,b*) The position of the nose $x_N(t)$ of bentonite currents with the ageing times $T_{age}$ indicated, on slopes of (*a*) 20° and (*b*) 24°. (*c*) The final distance travelled by the nose of the current $x_F$ as a function of the inclination angle, for the ageing times $T_{age}$ indicated. (*d*) The initial structure parameter $\lambda_0$ of the rheological model, as a function of the ageing time $T_{age}$, estimated from the data in (*c*), as discussed in the text.

of $T_{age}$, the final runout of the current $x_F$ increases steadily with inclination angle. For larger values of $T_{age}$, however, the runout increases suddenly over an increasingly narrow band of angles. The oldest sample, with $T_{age} = 1080$ min, exhibits extremely abrupt 'avalanching': at 20° the fluid remains stationary on the slope, but at 24° the fluid dramatically de-structures (after the delay illustrated in figure 13*b*) and flows off the bottom of the plate.

5.2.2. *Comparison of experiments and theory*

The experimental results exhibit many of the qualitative features predicted by the theoretical model. In particular, the effect of the ageing time is broadly similar. For small $T_{age}$ ($\lambda_0$ near 1/2), both theory and experiments show that the current behaves like a yield-stress fluid (cf. Coussot *et al.* 2005). Similarly, as $T_{age}$ or $\lambda_0$ increases, the currents develop a pronounced horseshoe of structured fluid at the back, a thinned interior, and a raised nose at the front. The experiments confirm the theoretical prediction of a critical angle below which there is little or no flow, which increases with $T_{age}$ (figure 13*c*). Above the critical angle, the fluid flows over a significant distance.

The slumps in the experiments are shallow relative to their lateral dimensions, in accordance with the lubrication framework of the theoretical model. However, near the fluid edge, the slope of the surface can become order one. Whilst this violates the

lubrication assumption locally, it is not clear how much of a qualitative effect this has on the evolution of the current elsewhere.

The experiments suggest rough estimates for some of the parameters of the theory: the radius of the initial slump on a horizontal plate in the experiments can be matched with the model prediction (4.8) to give an estimate of the critical yield stress of $\tau_C \approx 16$ Pa (the density of the bentonite was 1.07 g cm$^{-3}$). This is comfortingly close to the stress at which the lower viscosity bifurcation is seen in the cone-and-plate rheometry data in figure 1(*b*). (Our efforts to prepare an identical solution were not completely successful; simple slump tests showed that the sample used in the rheometry, which was performed in a different location, had a slightly thicker consistency than the samples used for the gravity-current experiments.)

We can also determine the critical angle as a function of the ageing time from the measurements shown in figure 13(*c*). By using the two-dimensional analysis of § 4.2.2, we can then estimate the absolute yield stress $\tau_A(T_{age})$. We find that $\tau_A$ increases from approximately 20 Pa at $T_{age} = 5$ min to ∼50 Pa at $T_{age} = 1080$ min. In comparison, the higher viscosity bifurcation in the rheometry data of figure 1 occurs at a stress just above 30 Pa, the material ageing for ∼6 min before yielding. Given that $\tau_A = [\Gamma\lambda_0(1-\lambda_0)]^{-1} = \tau_C/[4\lambda_0(1-\lambda_0)]$, the estimates for these critical stresses imply the relation $\lambda_0(T_{age})$ plotted in figure 13(*d*).

There are several notable differences between the experimental results and the theoretical predictions. For example, the theoretical final state is a thin and almost flat current, which is approached extremely slowly. In the experiments, however, the flow stops abruptly and the horseshoe remnant and raised nose still decorate the deposit. One possible explanation for this disagreement is that the theoretical final state is entirely controlled by $\tau_C$, whereas the re-structuring rheology of the bentonite is more complicated. In particular, our model ignores any material ageing during the late stages of the slump, which may be responsible for switching off the flow and leaving intact the structured remnant (as in the computations of Coussot *et al.* 2005, whose model allows for such an effect).

Another difference is that, in the theory, the total distance that the current flows is a function of the slope $S$ but is independent of $\lambda_0$ and thus of ageing, provided the slope is above the critical value. In the experiments, however, the total run-out distance is a function of both the slope and ageing time $T_{age}$ (figure 13*c*). On a 24° slope (figure 13*b*), the older samples even travel further than the younger ones. It is possible that the rapid acceleration of these samples introduces inertial effects which are not included in the theoretical model.

In both experiments and theory there is a delay before the nose of the current starts to flow when the angle is just above its critical value. This feature was noted previously by Huynh *et al.* (2005). In the theory, the delay is the lag experienced as the yielded sections of the fluid, which first appear at the centre of the initial dome but are dammed up by downslope structured fluid, migrate to the front. In the experiments, however, it is not so clear whether this is the underlying cause of the delay. Indeed, the delay time can be long compared with the time scales of the flow (see e.g. figure 13*b*); it is conceivable that time-dependent internal de-structuring is important, whereas it is instantaneous in the theoretical model.

Lastly, the experiments demonstrate that the fluid can de-structure even more dramatically than the model predicts, particularly if the ageing time is large. Figure 12(*c*), for example, shows an extreme degree of thinning in the interior of the current, which we have not been able to capture with our model. This difference is perhaps due to the detailed rheology; the viscosity, for example, may depend more

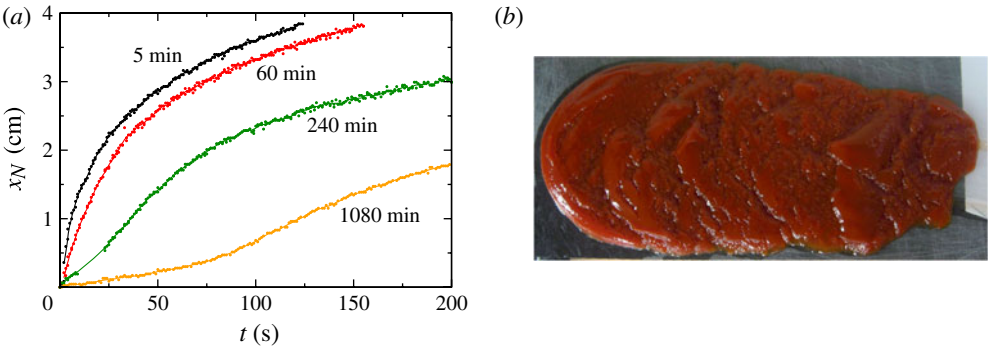


FIGURE 14. (Colour online) Experiments with Heinz tomato ketchup: (*a*) the position of the nose of the current $x_N(t)$ on a 14° slope for the ageing times indicated; (*b*) a photograph from above of a ketchup current (downslope is to the right), showing a structured horseshoe at the back (left), and significant surface texture on the rest of the current. The initial diameter of the ketchup was ∼13 cm.

sensitively on the strain rate. It could also be due to the neglect of extensional stresses in the structured fluid layer. As remarked earlier in § 4.1, we do not account for such extensional stresses, and the enhanced viscosity of the structured fluid only suppresses vertical shear. However, if the upper layer is sufficiently viscous, the extensional stresses can contribute to the force balance along with the shear stress (as in models of free viscous films or sliding ice sheets and shelves (cf. Balmforth, Craster & Toniolo 2003)). The inclusion of extensional stresses may lead to an increased thinning of the interior of the current and the fusion of the front and back into a rigid nose and horseshoe much like in the experiments, offering an intriguing avenue for further study.

### 5.3. *Ketchup*

We also carried out experiments using Heinz tomato ketchup. Ketchup is an interesting and complex multicomponent fluid, and is difficult to use experimentally due to its tendency to separate over time. In particular, ketchup readily expels vinegar, which gathers around the base of the sample if it is left at rest for more than a few minutes. Owing to this separation problem, we only very briefly discuss the results. We observed thixotropic behaviour which, in some respects, resembled the behaviour of bentonite. In particular, for ageing times $T_{age} \gtrsim 1$ h there was a clear horseshoe of structured ketchup left at the back of the ketchup current. As with bentonite (figure 13*b*), the evolution of the current changed qualitatively with ageing time: for long ageing times, the flow gradually accelerated from rest, in contrast to the behaviour for small $T_{age}$ (figure 14*a*).

However, the ketchup current differed in both appearance and behaviour. It proved difficult to observe dramatic avalanche behaviour with ketchup. The current also had no pronounced nose, nor did it thin over its interior. Interestingly, the current always continued to flow throughout the duration of the experiments, rather than coming to an abrupt halt like the bentonite. These observations highlight the complexity of thixotropic behaviour: the ketchup current shows clear ageing effects, even though it does not exhibit all the same phenomena as the bentonite. The photograph of a ketchup experiment in figure 14(*b*) shows the structured horseshoe remnant, and the gravity current extending down the slope. This picture also illustrates the complex

wavy structure of the surface of the current, which is perhaps the result of an interfacial instability like that which occurs in the theoretical model.

## 6. Conclusions

In this paper, we have presented a model for thixotropic gravity currents and compared its predictions with experiments using a solution of bentonite. There is broad qualitative agreement between theory and experiment, but there are also some interesting differences.

In our model, the degree of microstructure in the fluid is dictated by the local stress $\tau$ through a relation that allows for viscosity bifurcations at two critical yield stresses $\tau_A$ and $\tau_C$. Solid-like structured fluid can only de-structure and flow once the stress upon it exceeds the first critical stress $\tau_A$. Conversely, de-structured fluid abruptly re-structures back to the solid-like state if the stress falls below the second critical stress $\tau_C$ (or, equivalently, if the shear rate falls below the critical value $\dot{\gamma}_C$). By allowing $\tau_A$ to depend on the length of time the fluid has been left standing, we accommodate a dependence on the initial ageing time $T_{age}$. Our thixotropic law describes scenarios in which the evolution of the structure at the critical stresses is rapid and all other material ageing is slow, in comparison to the time scales of the flow.

For a mound of fluid placed on an inclined plane, if the local stress is nowhere above $\tau_A$, the fluid cannot yield. Hence there is a critical angle below which the fluid will not flow, which increases with ageing time. Above the critical angle, fluid de-structures and begins to move. The de-structured fluid remains yielded and continues to flow until the local stress falls below $\tau_C < \tau_A$. Consequently, the current flows significantly once the critical angle is exceeded. With longer ageing times, the critical stresses $\tau_A$ and $\tau_C$ become more separated, increasing the critical angle and the degree of thinning once this threshold is exceeded. The flow also becomes increasingly characterized by a raised nose at the fluid front and a remnant of structured fluid at the back, which, in three dimensions, takes the shape of a horseshoe. Experiments with bentonite clay show qualitative similarities with all these features of the dynamics.

The theory and experiments differ most notably in their final states: in the theory the flow slowly evolves to an almost flat profile, with the raised nose remnant at the back slowly eroding away over a very long time scale. In the experiments, however, the bentonite came to an abrupt halt with a persistent raised nose and horseshoe. The experimental flows also thin more dramatically than those of the model. These discrepancies could be due to the neglect of extensional stresses of the structured fluid in the model, or a more complicated time-dependent thixotropic rheology.

## Acknowledgements

The majority of this work took place during the 2012 Geophysical Fluid Dynamics summer program at Woods Hole Oceanographic Institution, which is supported by the National Science Foundation and the Office of Naval Research. We thank the directors, staff and fellows of the program, and particularly A. Jensen for his assistance with the experiments. We thank the referees for constructive comments on an earlier draft of this manuscript.

## Appendix. Interfacial instability

Superposed, inclined shallow layers of Newtonian (Chen 1993) or power-law (Balmforth *et al.* 2003) fluid with differing viscosities can be unstable to an interfacial

instability, even in the absence of inertia. An analogous instability arises in our model for a thixotropic gravity current when the yield surface is a material curve separating structured fluid above from de-structured fluid below. In this Appendix, we explore the instability for the simpler problem of a uniform shallow sheet in two dimensions, assuming that the yield surface remains separated from $z = z_A$ and $z = z_C$. The governing equations (3.14)–(3.18) are then

$$\frac{\partial h}{\partial t} + \frac{\partial}{\partial x} F(h, h_x, Y) = 0, \quad \frac{\partial Y}{\partial t} + \frac{\partial}{\partial x} G(h, h_x, Y) = 0, \tag{A 1a,b}$$

where

$$F(h, h_x, Y) = \int_0^h u \, \mathrm{d}z = (S - h_x) \int_0^Y (h - z)^2 \, (1 - \lambda) \, (1 - \lambda/\lambda_0) \, \mathrm{d}z, \tag{A 2}$$

$$G(h, h_x, Y) = \int_0^Y u \, \mathrm{d}z = (S - h_x) \int_0^Y (h - z) \, (Y - z) \, (1 - \lambda) \, (1 - \lambda/\lambda_0) \, \mathrm{d}z, \tag{A 3}$$

and the subscript on $h_x$ refers to a partial derivative. The fluxes $F$ and $G$ can be evaluated analytically using

$$\lambda = \lambda_- = \frac{1}{2} \left[ 1 - \left( 1 - \frac{4}{\Gamma \, (h - z) \, (S - h_x)} \right)^{1/2} \right], \tag{A 4}$$

which comes from (2.5*b*).

Equations (A 1) have the uniform equilibrium solution $h = h_0$ and $Y = Y_0$. Normal-mode perturbations to this base state of the form $\mathrm{e}^{\sigma t + \mathrm{i}kx}$, with wavenumber $k$ and growth rate $\sigma$, satisfy a dispersion relationship

$$\sigma^2 + \sigma \left( Ak^2 + \mathrm{i}Bk \right) + \mathrm{i}Ck^3 + Dk^2 = 0, \tag{A 5}$$

where

$$A = \frac{\partial F}{\partial h_x}, \quad B = \frac{\partial F}{\partial h} + \frac{\partial G}{\partial Y}, \quad C = -\frac{\partial G}{\partial h_x} \frac{\partial F}{\partial Y}, \quad D = \frac{\partial G}{\partial h} \frac{\partial F}{\partial Y} - \frac{\partial G}{\partial Y} \frac{\partial F}{\partial h}, \tag{A 6a,b,c,d}$$

all evaluated at $h = h_0$, $Y = Y_0$, and $h_x = 0$. It follows from (A 5) that $\mathrm{Re}\{\sigma\} = 0$ only if $k = 0$; that is, the uniform flow is either unstable or stable for all wavenumbers. For $k \gg 1$, we find the two solutions,

$$\mathrm{Re}\{\sigma_1\} = -Ak^2 + O(1), \quad \mathrm{Re}\{\sigma_2\} = \frac{C^2 - ABC - A^2 D}{A^3} + O(k^{-1}). \tag{A 7a,b}$$

On examining the partial derivatives of $F$ and $G$ in more detail, one can establish that the first solution is stable ($A > 0$) whereas the second can be unstable (if $C^2 - ABC - A^2 D > 0$). With a little more effort, one can show that the growth rate of the unstable solution increases monotonically from zero at $k = 0$ up to the constant maximum given by (A 7*b*), and has finite phase speed $c = -\mathrm{Im}\{\sigma\}/k$. With parameter settings guided by the full slump problem considered in the main text, it turns out that the growth rate of instability is typically relatively small in magnitude, rather less than the corresponding phase speed. Hence, the perturbations propagate much faster than they grow. Typical solutions of (A 5) are shown in figure 15(*a*).

The system (A 1) can also be solved numerically with periodic boundary conditions to explore the nonlinear dynamics of the interfacial instability, starting from a small perturbation to the uniform base flow. Figure 15(*b,c*) shows the results of such

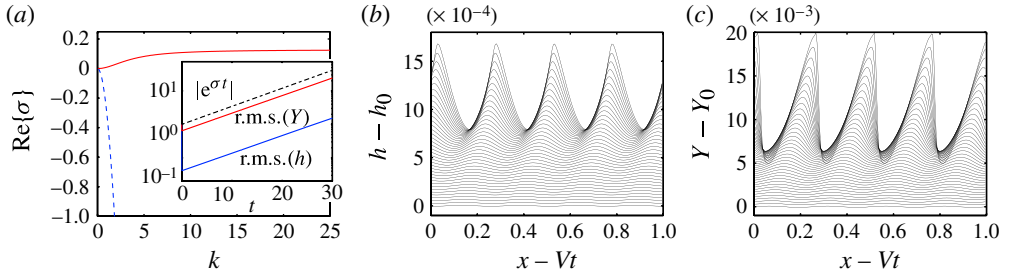


FIGURE 15. (Colour online) Interfacial instability of a uniform sheet for $\Gamma = 40$, $\lambda_0 = 0.9$, $h_0 = 1$ and $Y_0 = 0.5$. (*a*) shows the unstable (solid) and stable (dashed) roots of the dispersion relationship (A 5). (*b–c*) show numerical solutions for $h$ and $Y$, respectively, from an initial-value problem beginning with the uniform flow plus a small perturbation with wavenumber $8\pi$ and the spatial form of the unstable normal mode. The solutions are plotted at each time unit and vertically offset, in a frame moving at a speed $V$ close to the modal phase speed. Note the different vertical scales in (*b,c*). The inset of (*a*) shows the r.m.s. values of $h - h_0$ and $Y - Y_0$ against time, along with the trend of the unstable mode.

an initial-value computation, starting with a perturbation with wavenumber $k = 8\pi$, corresponding to four waves. The instability develops as predicted by linear theory and is more prominent on the yield surface than on the free surface. In the nonlinear regime, the instability leads to the formation of shocks on the material yield surface, with the same wavenumber as the original perturbation. These shocks generate high-wavenumber oscillations on the scale of the grid, which is probably an artefact of the numerical scheme used to solve the equations. The short-wave character of the instability also compromises the shallow-layer assumption inherent in lubrication theory; it is likely that extensional stresses would introduce a short-wavelength cut-off, removing the generation of overly fine wavelengths.

## REFERENCES

ALEXANDROU, A. N., CONSTANTINOU, N. & GEORGIOU, G. 2009 Shear rejuvenation, aging and shear banding in yield stress fluids. *J. Non-Newtonian Fluid Mech.* **158**, 6–17.

BALMFORTH, N. J. & CRASTER, R. V. 1999 A consistent thin-layer theory for Bingham plastics. *J. Non-Newtonian Fluid Mech.* **84**, 65–81.

BALMFORTH, N. J., CRASTER, R. V., PERONA, P., RUST, A. C. & SASSI, R. 2006*a* Viscoplastic dam breaks and the Bostwick consistometer. *J. Non-Newtonian Fluid Mech.* **142**, 63–78.

BALMFORTH, N. J., CRASTER, R. V., RUST, A. C. & SASSI, R. 2006*b* Viscoplastic flow over an inclined surface. *J. Non-Newtonian Fluid Mech.* **139**, 103–127.

BALMFORTH, N. J., CRASTER, R. V. & SASSI, R. 2002 Shallow viscoplastic flow on an inclined plane. *J. Fluid Mech.* **470**, 1–29.

BALMFORTH, N. J., CRASTER, R. V. & TONIOLO, C. 2003 Interfacial instability in non-Newtonian fluid layers. *Phys. Fluids* **15**, 3370–3384.

BARNES, H. A. 1997 Thixotropy – a review. *J. Non-Newtonian Fluid Mech.* **70**, 1–33.

BONN, D., TANAKA, H., COUSSOT, P. & MEUNIER, J. 2004 Ageing, shear rejuvenation and avalanches in soft glassy materials. *J. Phys.: Condens. Matt.* **16**, S4987–S4992.

CHEN, K. P. 1993 Wave formation in the gravity-driven low Reynolds number flow of two liquid films down an inclined plane. *Phys. Fluids* A **5**, 3038.

COUSSOT, P., NGUYEN, Q. D., HUYNH, H. T. & BONN, D. 2002*a* Avalanche behaviour in yield stress fluids. *Phys. Rev. Lett.* **88**, 175501.

COUSSOT, P., NGUYEN, Q. D., HUYNH, H. T. & BONN, D. 2002*b* Viscosity bifurcation in thixotropic, yielding fluids. *J. Rheol.* **46**, 573–589.

COUSSOT, P., ROUSSEL, N., JARNY, S. & CHANSON, H. 2005 Continuous or catastrophic solid–liquid transition in jammed systems. *Phys. Fluids* **17**, 011704.

DULLAERT, K. & MEWIS, J. 2006 A structural kinetics model for thixotropy. *J. Non-Newtonian Fluid Mech.* **139**, 21–30.

HENRIQUEZ, J. & SIMMS, P. 2009 Dynamics imaging and modelling of multilayer deposition of gold paste tailings. *Minerals Engng* **22**, 128–139.

HUPPERT, H. E. 1982 The propagation of two-dimensional and axisymmetric viscous gravity currents over a rigid horizontal surface. *J. Fluid Mech.* **121**, 43–58.

HUYNH, H. T., ROUSSEL, N. & COUSSOT, P. 2005 Ageing and free surface flow of a thixotropic fluid. *Phys. Fluids* **17**, 033101.

KHALDOUN, A., MOLLER, P., FALL, A., WEGDAM, G., DE LEEUW, B., MÉHEUST, Y., FOSSUM, J. O. & BONN, D. 2009 Quick clay and landslides of clayey soils. *Phys. Rev. Lett.* **103**, 188301.

LISTER, J. R. 1992 Viscous flows down an inclined plane from point and line sources. *J. Fluid Mech.* **242**, 631–653.

LIU, K. F. & MEI, C. C. 1989 Slow spreading of a sheet of Bingham fluid on an inclined plane. *J. Fluid Mech.* **207**, 505–529.

MEWIS, J. & WAGNER, N. J. 2009 Thixotropy. *Adv. Colloid Interface Sci.* **147–148**, 214–227.

MOLLER, P., FALL, A., CHIKKADI, V., DERKS, D. & BONN, D. 2009 An attempt to categorize yield stress fluid behaviour. *Phil. Trans. R. Soc. Lond.* A **367**, 5139–5155.

MOLLER, P., MEWIS, J. & BONN, D. 2006 Yield stress and thixotropy: on the difficulty of measuring yield stress in practice. *Soft Matt.* **2**, 274–283.

PUTZ, A. M. V. & BURGHELEA, T. I. 2009 The solid–fluid transition in a yield stress shear thinning physical gel. *Rheol. Acta* **48**, 673–689.

SIMMS, P., WILLIAMS, M. P. A., FITTON, T. G. & MCPHAIL, G. 2011 Beaching angles and evolution of stack geometry for thickened tailings – a review. In *Paste 2011 Proceedings of the 14th International Seminar on Paste and Thickened Tailings, Perth, Australia* (ed. R.J. Jewell & A.B. Fourie), pp. 323–338.